Experimental Thermal and Fluid Science 146 (2023) 110931

Contents lists available at ScienceDirect

Experimental Thermal and Fluid Science

journal homepage: www.elsevier.com/locate/etfs

Extensional flow for assessing the effect of nanocarriers on the mechanical deformability of red blood cells

Jana Kriebel [a,d,e], Inês M. Gonçalves [b,c], Vitória Baptista [d,e,f,g], Maria I. Veiga [f,g], Graça Minas [d,e], Rui Lima [b,h,i], Susana O. Catarino [d,e,*]

[a] City University of Applied Sciences, Hochschule Bremen, School of Nature and Engineering, Neustadtswall 30, 28199 Bremen, Germany
[b] METRICS, University of Minho, School of Engineering, Campus de Azurém, 4800-058 Guimarães, Portugal
[c] IN+—Center for Innovation, Technology and Policy Research, Instituto Superior Técnico, Universidade de Lisboa, Avenida Rovisco Pais, 1049-001 Lisboa, Portugal
[d] Microelectromechanical Systems Research Unit (CMEMS-UMinho), School of Engineering, University of Minho, Campus de Azurém, 4800-058 Guimarães, Portugal
[e] LABBELS – Associate Laboratory, Braga/Guimarães, Portugal
[f] Life and Health Sciences Research Institute (ICVS), School of Medicine, University of Minho, Campus de Gualtar, 4710-057 Braga, Portugal
[g] ICVS/3B's – PT Government Associate Laboratory, Braga/Guimarães, Portugal
[h] CEFT, Faculty of Engineering, University of Porto, 4200-465 Porto, Portugal
[i] ALiCE, Faculty of Engineering, University of Porto, 4200-465 Porto, Portugal

ARTICLE INFO

Keywords:
Deformation index
Microfluidics
Nanoparticles
Red blood cells
Extensional flow velocity

ABSTRACT

The effect of nanoparticles on the mechanical behavior of red blood cells (RBCs) under an extensional flow has not been extensively studied. In this work, by using a microfluidic hyperbolic contraction, it is assessed the deformability of healthy RBCs in contact with ~20 nm nanoparticles of magnetic iron and non-magnetic cerium. The results showed that, under a controlled extensional flow, the healthy RBCs deformability index depended on the cells' velocity along the microfluidic contraction. Additionally, the results showed that the deformability index of the RBCs decreased when the cells got in contact with the nanoparticles, being that difference higher for the magnetic nanoparticles and for the longer exposition times. The RBCs presented a logarithmic deformability index vs velocity trend, with variations according to the magnetic or non-magnetic properties of the nanoparticles, to the concentration and to the exposure time. Thus, the representation of the deformation index as a function of velocity seems to be a promising method to evaluate the mechanical behavior of the cells. Such knowledge will be essential for further understanding how the cell-nanoparticle interactions occur in RBCs disorders, and will open new possibilities regarding future applications of these nanocarriers in targeted drug delivery systems for therapeutics.

1. Introduction

The blood flow and the ability of the red blood cells (RBCs) to deform are indicators of many pathological conditions, as arterial hypertension, brain and cardiac infarctions, inflammation, diabetes or malaria, among other hemoglobinopathies [1–6]. Microfluidic devices have been widely explored for precise, low-cost, portable, continuous and high-throughput analysis of RBCs, and have becoming attractive clinical tools for rapid and efficient manipulation and characterization of blood samples, with potential use in diagnosis [4,7]. In microcirculation, the blood flows through extremely small vessels, including capillaries below 8 μm diameter [8], and this flow is strongly influenced by the mechanical deformability of the RBCs, as they make up almost half of the total blood composition. Additionally, hemoglobin is the main component of RBCs and makes up about 95 % of the proteins in the cytosol, reaching a concentration of about 5 mM in the cytoplasm [9]. When RBCs are suspended in an isotonic medium (such as plasma or physiological saline), they have a biconcave, discoid shape with a major diameter of about 6–8 μm [7]. When the healthy RBCs are exposed to large external flow forces, as it occurs when the cells face narrow capillaries or microfluidic devices with micro-contractions, they deform without rupturing, being able to cross those micro vessels, and usually return to their original shape when the external forces are removed [4,7]. Pathological RBCs usually have a lower ability to deform [3,4]

* Corresponding author at: Microelectromechanical Systems Research Unit (CMEMS-UMinho), School of Engineering, University of Minho, Campus de Azurém, 4800-058 Guimarães, Portugal.
E-mail address: scatarino@dei.uminho.pt (S.O. Catarino).

https://doi.org/10.1016/j.expthermflusci.2023.110931
Received 10 January 2023; Received in revised form 17 April 2023; Accepted 18 April 2023
Available online 23 April 2023

and to recover their biconcave shape [4].

In parallel, during therapeutics, the drug efficiency and the global spread of drug resistance [10–12] have become a challenge in the treatment of different diseases. In recent years, much research has been focused on targeted nanocarriers as alternatives for local drug delivery, to increase the drugs' efficiency. One promising option are nanoparticles (NPs), with high specificity, based on targeting properties present only on diseased/infected blood cells (as modifications in pH [13,14], temperature [15] or magnetic response [16–18], among others) [19]. Particularly, magnetic nanoparticles (MNPs) could be interesting in this area, as several diseases (for instance malaria, which leads to the formation and growing of hemozoin, a ferrous and paramagnetic crystal [20]) cause alterations in the magnetic properties of the RBCs [21,22].

Few studies report the influence of NPs on the RBCs deformation and flow for biomedical applications [21,23–26]. Rodrigues et al. (2016) [23] evaluated the RBCs deformability in contact with iron oxide MNPs, by using a polydimethylsiloxane (PDMS) microfluidic device with hyperbolic contractions to force an extensional flow, and detected small variations in the RBCs' stiffness and deformability index when MNPs bound to the cells [23,24]. In the reported study, the iron oxide MNPs, besides magnetic, were chosen as they have high surface-to-volume ratio, field irreversibility, high saturation magnetization, biocompatibility and non-toxicity, which are, indeed, remarkable nanoscale properties for biomedical applications [18,27,28].

It was predicted, as a research hypothesis, that healthy RBCs in contact with NPs suffer modifications in their mechanical behavior and deformation ability, and this effect will be higher as the NPs concentration and contact time increases. Thus, herein, following the Rodrigues et al. (2016) approach [23], we intend to study, using microfluidic platforms, how healthy RBCs mechanically respond to different magnetic iron oxide (Fe_3O_4) and non-magnetic cerium (CeO_2) nanocarriers, assessing the cells-nanoparticles affinity (through measuring the cells deformability), and exploring their potential for the future development of highly specific local drug delivery systems. The adsorption of NPs onto the surface of RBCs is strongly influenced by electrostatic interactions [29–31], and this attachment is higher for the more positively charged NPs and lower for negatively charged NPs (occurring repulsion), due to the electrostatic interactions with the negatively charged cells' membrane [29–31]. Additionally, due to their small size, some NPs are also able to cross the cells' membrane and translocate into the RBCs, although this mechanism is not entirely understood yet [32,33]. Thus, in this work, we will compare the effect between positively charged Fe_3O_4 NPs and negatively charged CeO_2 NPs. Additionally, as non-oxygenated hemoglobin molecules (ferrohemoglobin) present 4 unpaired electrons per heme, it confers them magnetic susceptibility and a pronounced paramagnetic contribution, with a magnetic moment of 5.46 μB/heme, as discussed in [34,35]. So, in this work it is also intended to evaluate if this minimal paramagnetic behavior has any effect on the binding of the RBCs to magnetic NPs flowing in microdevices, and if there are differences between the effect of magnetic and non-magnetic NPs.

It is expected that this work helps us to establish the basics of the interactions between RBCs and NPs and how these interactions affect the cells deformability, here with a focus on healthy RBCs. Such knowledge will be the first step for further understanding how those interactions occur in RBCs disorders and will open new possibilities regarding future applications in hemoglobinopathies, but also targeted drug delivery systems for cancer, malaria, cardiovascular diseases therapeutics, among others [19,36–38].

2. Methods

2.1. Samples preparation

A Dextran 40 (Dx40, chemical formula $(C_6H_{10}O_5)_n$) solution (Sigma-Aldrich, USA) containing RBCs at a 0.1 % of hematocrit was used as the working fluid in the microfluidic experiments. Blood was provided by healthy individuals by the *Instituto Português do Sangue e da Transplantação* (IPST) – Porto. The blood samples were collected into 2.7 mL tubes (S-Monovette®, Sarstedt) filled with ethylenediaminetetraacetic acid (EDTA). All procedures for the collection of blood and for the in vitro experiments were carried out in compliance with the EU directives 2004/23/CE, 2006/17/CE. The RBCs were obtained from whole blood by three centrifugation steps, in a Centrifuge (XC-2009, Premiere, USA), for 15 min at 1500 rpm, at room temperature. Between each centrifugation step, the supernatant was removed and the RBCs were re-suspended and washed in a physiological salt solution (PSS) with 0.9 % NaCl (supplied by B. Braun Medical, Germany), in a 1:1 ratio. This step intended to separate the RBCs from plasma and the buffy coat. Afterwards, the collected RBCs were added to the D×40 solution in a 0.1 % concentration. D×40 was used as carrier fluid instead of blood plasma to avoid the clotting and jamming of the blood cells in the in vitro microfluidic studies, which are generally promoted by some blood components [23]. Experiments were conducted with two different concentrations (0.1 % and 0.01 %) of positively charged magnetic iron oxide (Fe_3O_4) [39] and negatively charged nonmagnetic cerium (CeO_2) nanoparticles (NPs), both types of NPs with diameter around 18–20 nm. The protocol synthesis of the magnetic iron NPs (Fe-MNPs) is detailed in Rodrigues et al. (2016) [23], and the synthesis of the non-magnetic cerium NPs (Ce-NPs) followed the protocol described by Mahmoud and Faidah (2012) [40], via a microwave assisted hydrothermal technique in the presence of different amounts of poly vinyl pyrrolidone (PVP) [40], where the use of PVP in the synthesis is responsible for conferring the negative charge to the NPs (as described in [41]). Additionally, the Fe-MNPs were functionalized with hydrophilic ligands by adding alendronic acid into the colloidal suspensions, followed by sonication, stirring and purification, assuring the colloidal stabilization of the ferrofluids, and avoiding their agglomeration and fast sedimentation. After synthesis of the NPs, the NPs and the Dx40 + RBCs solution were weighed using a micro analytical balance (BBC32, Boeco, Germany), to add a mass percent of 0.1 % and 0.01 % of Fe-MNPs or Ce-NPs to the working fluid. The microfluidic experiments were performed 1 h and 72 h after the preparation of the working fluid. Between experiments, the working fluid was stored in the fridge at 8.5 °C. During the entire refrigerator storing time, the RBCs were kept suspended in the Dx40 carrier fluid, to avoid the cells' hemolysis, also avoiding clotting, jamming and sedimentation. Nevertheless, before each extensional flow assay (both at 1 h and at 72 h), the integrity of the RBCs samples was observed at the microscope, to assure that no hemolysis occurred [42,43] and the cells' mechanical behavior could be captured.

2.2. Microchannels fabrication

Polydimethylsiloxane (PDMS) microchannels with geometric contractions were microfabricated using soft lithography with epoxy-based negative photoresist (SU-8) molds, as reported in [44]. PDMS is transparent (allowing optical and microscopy measurements) and allows surface functionalization by O_2 plasma surface treatment [4,45]. The geometry and main dimensions of the microchannels are shown in Fig. 1. The microchannels comprise an inlet for the RBCs samples, an outlet region and a hyperbolic micro-contraction area, with 20 μm width to force the RBCs to deform [4,45,46]. Each channel has a 20 μm height, and contains a hyperbolic-shaped contraction with a total length of 400 μm, and a minimum width at the end of the contraction region of 20 μm (similar to the diameter of various blood vessels and capillaries in microcirculation). The width of the microchannel, before and after the contraction region, is 400 μm. The hyperbolic-shaped contraction [47–49] with a Hencky strain of ~3 (also called logarithmic strain, $\epsilon_H = \ln(W_{Max}/W_{Min})$) [50] was used to allow the velocity to increase almost linearly with the axial position × (constant strain rate), without suffering entrance or exit effects, being adequate for a better control of the microflows, and with lower risk of clogging [23,50].

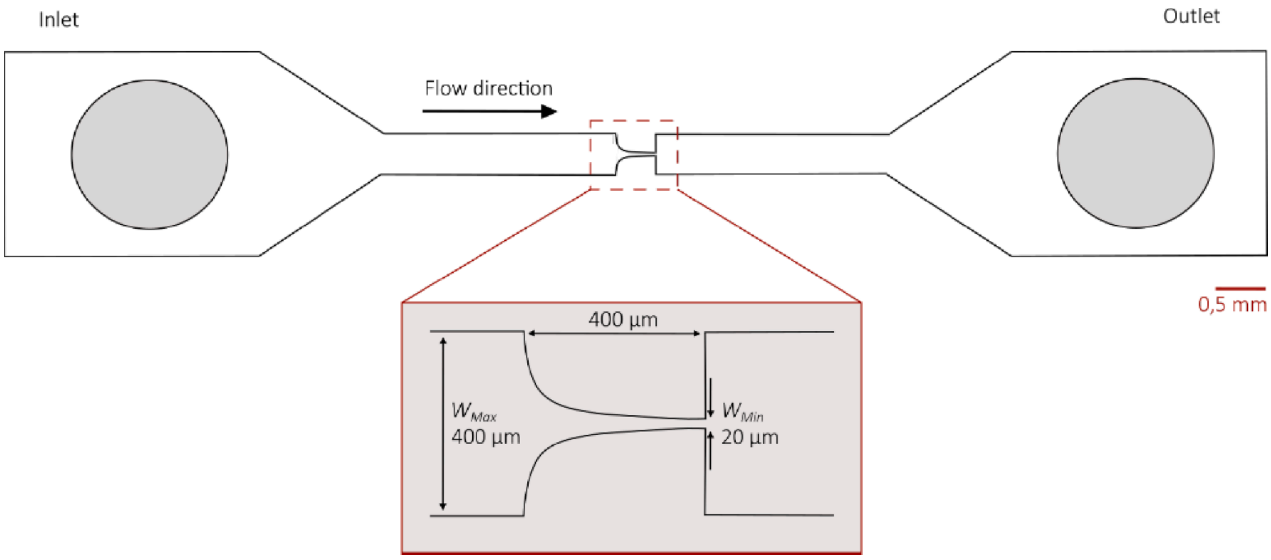

Fig. 1. Geometry of the microchannel used in the experiments. The samples flow through a tube into the microchannel on the inlet side (grey area), pass through a pre-contraction region, through the channel hyperbolic contraction and exit through the post-contraction/relaxation area to the outlet side (grey area). The channel depth, d, is 20 µm. The width before and after the hyperbolic contraction region is the same, $W_{Max} = 400$ µm. The minimum width in the contraction region is $W_{Min} = 20$ µm, defining a total Hencky strain of 3. The total length of the microchannel is 1.25 cm.

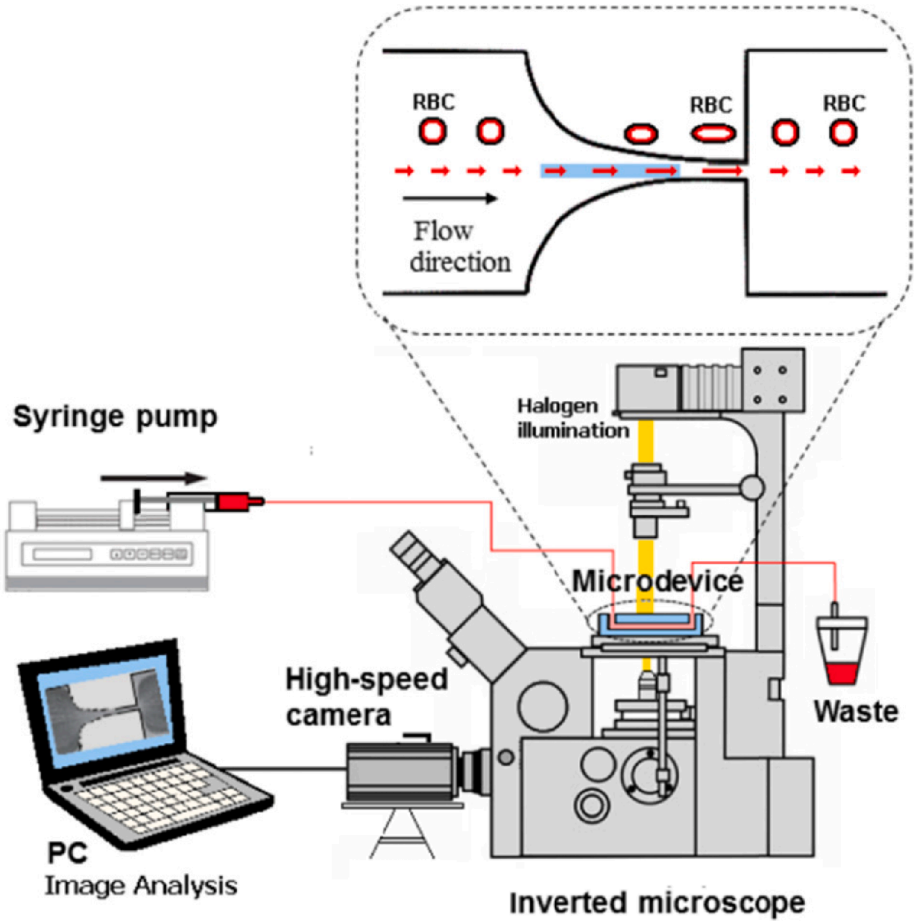

Fig. 2. Schematic diagram of the experimental setup. The setup consists of a syringe pump connected to the microchannel through polymeric tubing. The microfluidic device is fixed on an inverted microscope. A high-speed camera is connected to the microscope and to the computer for data acquisition. Adapted from [51], distributed under a Creative Commons Attribution License (CC BY 4.0).

2.3. Measurement setup and data analysis

For the microfluidic experiments, the 0.1 % hematocrit RBCs samples (with and without NPs) were filled into a syringe pump (Nemesys B101-02 D, Cetoni, Germany). The syringe pump was connected to the entry of the microchannel and ensured a controlled inflow of the sample into the channel. At the exit of the microchannel, the fluid was disposed. The inlet flow rate was kept constant at 20 μL/min. The microfluidic device was fixed on the stage of a microscope (IX71, Olympus, Japan). The magnification used in all experiments was 10 × by the objective + 1.6 zoom of the microscope. A high-speed camera (Fastcam SA3, Photron, Japan) was connected to the microscope and recorded pictures (1024 × 256 px resolution) of the flowing RBCs, with a frame rate of 7500 fps and 1/30000 s exposure time. Finally, the high-speed camera was connected to a computer for data acquisition, using Photron Fastcam Viewer software (3282(×64), Photron, Japan). Fig. 2 presents a schematic of the entire microfluidic setup. All experiments were performed at room temperature. It is important to notice that the spatial resolution of the acquired frames results from a balance between the frame rate (which needs to be high to follow and measure the high velocity of the individual RBCs inside the contraction) and the image quality, as improving one of them decreases the quality of the other.

The recorded videos were analyzed with the image handling software ImageJ (1.53 k, NIH, USA). Fig. 3 shows the complete process of analyzing a frame in ImageJ. First, the videos were converted into a stack of static frames, as in Fig. 3 a). Then, a background image was created, based on the average of all frames from one video, through the *ZProject* function, as seen in Fig. 3 b). The background picture was then subtracted from all frames to eliminate all noise and static objects (including the microchannel walls), resulting in frames containing only the flowing RBCs, as seen in Fig. 3 c). At this stage, the image quality of the frames was improved through Brightness/Contrast adjustment filters and Median operation filters (in which a radius of 1 pixel was applied). Afterwards, the frames were converted into binary images using the Otsu threshold method. This resulted in images with the RBCs as white, elliptical objects against a black background, as shown in Fig. 3 d).

As a next step, 10 RBCs from each video were randomly selected and their movement was manually tracked frame by frame. As the RBCs flow in the channel, at standard distances to the entrance of the contraction (see Fig. 4 a)), the RBCs major (X) and minor (Y) axis length, the x and y coordinates of their centroid and their area were measured using the ImageJ measurements *Fit ellipse*, *Centroid* and *Area* functions. The resulting datasets were saved and served as the basis for calculating the deformation index (DI) of the RBCs, through the expression: $DI = (X\text{-}Y)/(X + Y)$, where $0 < DI < 1$. The higher the DI, the higher the cell elongation. A second series of measurements was taken in ImageJ to determine the velocity of the RBCs, by using the MTrackJ plugin and tracking the same 10 RBCs from each video, frame by frame. All collected data ($n = 10$) were combined, resulting in the given DI and velocity for each randomly selected RBC, at different time instants and positions in the microchannel.

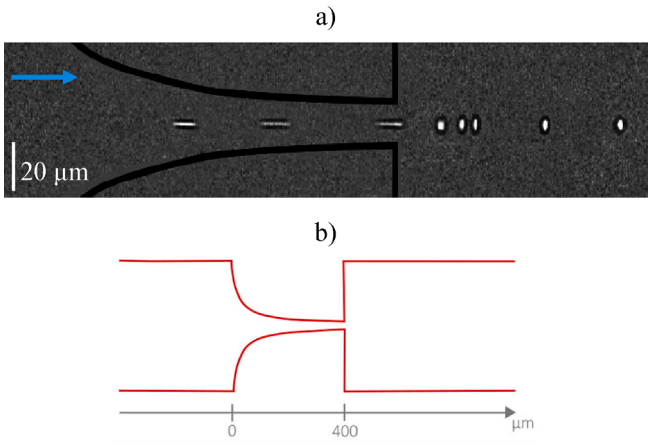

Fig. 4. a) Example of the deformation of a healthy RBC at the end of the contraction region, where the blue arrow indicates the flow direction, obtained by overlapping several frames of the video. The RBC first deforms strongly in the horizontal direction, and after the sudden end of contraction it resumes its original shape before deforming again, more slightly, in the vertical direction. At the end, it recovers its original shape. **b)** Hyperbolic contraction geometry, with reference to the distance to the beginning of the contraction (point 0 of the *x*-axis).

3. Results and discussion

3.1. RBCs tracking

Under an extensional flow, as the RBCs pass the hyperbolic contraction, they gain velocity and are forced to deform and elongate inside the contraction, increasing significantly their DI, and recovering their original concave shape (more circular) after the expansion area, as seen in the example presented in Fig. 4a). Fig. 4b) presents a schematic representation of the hyperbolic geometry, where the x axis position represents the distance to the beginning of the contraction, as will be used as reference for the results presented in the subsequent DI plots.

As it can be seen in Fig. 4, the RBCs resolution, although allowing to observe the cells' deformation, is not perfect. It is important to point out that, although the manual tracking and measuring of the RBCs deformability is a common and widely reported methodology in bio-microfluidics (as in [4,46,52]), it is a highly time consuming method and has several limitations, both on image acquisition and data processing. In particular, human errors may result from the manual selection of RBCs at each microscope frame (as it ideally should be purely random and automatic) and from the manual adjustment of the focus plan for the images' acquisition. Additionally, due to the high velocity of the cells under an extensional flow, the acquisition setup (namely the high-speed

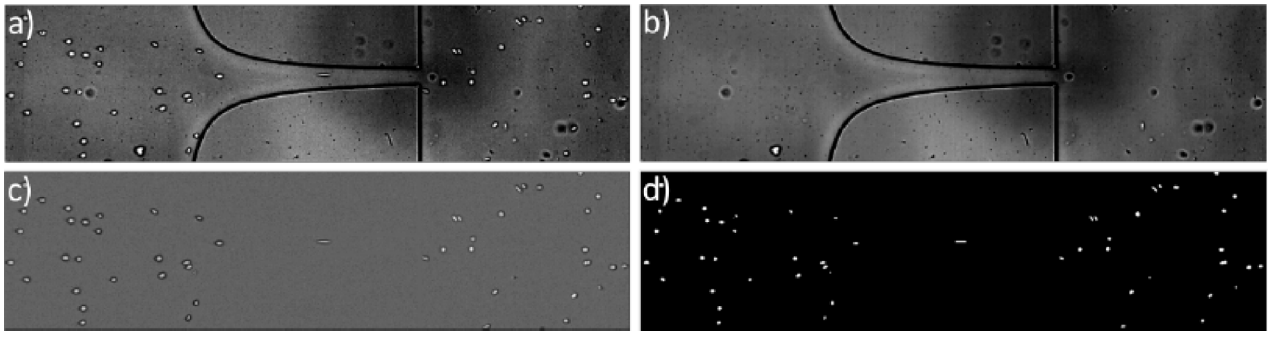

Fig. 3. Intermediate results of the image analysis steps in ImageJ: **a)** Single frame, after converting the video into static images; **b)** Background image from all the frames of one video; **c)** Result after subtracting the background from the frame a); **d)** Binary frame after using the threshold settings.

camera and objective lens) suffers from limitations which severely affect the image spatial resolution. On one side, the frame rate needs to be extremely high to follow and measure the behavior of individual cells flowing through the contraction. By increasing the frame rates, the illumination is reduced and, as a result, the image quality also decreases. On the other side, to measure the cells deformability at such high velocities, we have to use a 10× objective lens with a lower numerical aperture, which also reduces the image resolution. Both of these factors may increase the difficulty when measuring the major and minor axis length of each cell, potentially affecting the precision of DI measurements.

Fig. 5 summarizes the variation of the deformation index (a.u.) and particle velocity (cm/s) of randomly selected RBCs as a function of the distance (μm) to the beginning of the contraction, for healthy RBCs without NPs, for RBCs with Fe-MNPs at 0.01 % and 0.1 % concentrations and for RBCs with Ce-NPs at the same concentrations. In particular, Fig. 5a) presents the DI measured 1 h after the preparation of the samples, and Fig. 5b) presents the same data, 72 h after the preparation of the samples. Fig. 5c) and d) present the velocity of the same samples, measured 1 h and 72 h after the preparation of the samples, respectively. For consistency purposes, all the data presented from samples containing only RBCs and Dx40 are labelled as RBC, and the data obtained from samples containing NPs are labelled RBC plus the corresponding concentration and type of NPs (RBC + Fe-MNPs or Ce-NPs, respectively).

As it can be seen in Fig. 5a), a random 1 h healthy RBC (short storage time) starts to elongate even before the beginning of the hyperbolic contraction (as seen in Fig. 4, $x = 0$ represents the beginning of the contraction), and reaches the highest DI and velocity at the end of the contraction ($x = 400$ μm). While the velocity of the RBC increases linearly until the end of the contraction, the DI shows an approximately quadratic increase. After the sudden end of the contraction, both the velocity and the DI fall back to their initial values and the RBCs resume their original shape. At that point, the velocity remains constant, while the DI, under certain conditions (more evident after 1 h, for healthy and Ce-NPs RBCs), increases again, more slightly, as it can be seen in Fig. 5a), on the second DI peak between 400 and 600 μm. Analyzing Fig. 4a), we can observe that, while the main deformation region relates to a x axis elongation, the second area, with a less prominent deformation region, relates to a y axis deformation of the RBCs, probably due to the rotation of the cells while recovering their original shape at low velocity.

From the DI data presented in Fig. 5, it is visible that the RBC + Ce-NPs sample (non-magnetic sample) has a mechanical behavior similar to the healthy RBCs, for both nanoparticle concentrations, at 1 h and 72 h. However, regarding the RBC + Fe-MNPs sample (magnetic), it has a different DI profile as a function of the distance to the beginning of the contraction. Observing the data from 1 h after sample preparation, these RBCs start to deform later than the healthy and non-magnetic samples (around 100 μm after the beginning of the contraction) and for a shorter distance, and that delay is higher as the Fe-MNPs concentration increases. Also, this sample reaches a lower maximum deformation than healthy RBCs and RBCs with Ce-NPs, and does not present a second deformation area between 400 and 600 μm. These results indicate that magnetic Fe-MNPs may have a greater affinity and bound to the RBCs, affecting their deformability more than the non-magnetic Ce-NPs (where there is almost no difference in comparison with the healthy RBCs). These results are in agreement with the expected behavior of the electrostatic interactions between the NPs and the RBCs' membrane [29,30]. As the used Fe-MNPs are positively charged [39], while the Ce-NPs are negatively charged [41], the electrostatic interactions between the Fe-MNPs and the RBCs' negatively charged membrane [29] are higher than between the Ce-NPs and the RBCs.

Regarding the RBCs velocity, it has a major impact on the cells' deformation and, thus, it is important to be able to control it. The data from Fig. 5 shows that the hyperbolic contraction in the microchannel allows a linear increase of the velocity along the contraction, before its abrupt reduction, as already reported by [47,50]. Additionally, velocity does not seem to be affected by the nanoparticles binding, as the majority of the curves are superimposed, both for 1 h and 72 h after samples' preparation, indicating that, as expected, the velocity is dependent only on the applied flow rate (20 μL/min) and hyperbolic geometry (which is similar for all conditions).

Besides comparing the effect of magnetic/non-magnetic nanoparticles, it is also important to discuss the effect of the time after preparing the samples, as it is known that RBCs tend to become more rigid over time. For a better analysis of the effect of the binding time between the RBCs and the nanoparticles, Fig. 6 presents, for each sample, the deformation index (a.u.) of the RBCs presented in Fig. 5, as a function of the distance (μm) to the beginning of the contraction, at 1 h and 72 h after sample preparation. The results after 72 h show that healthy RBCs and RBCs with Ce-NPs still deform and achieve a high elongation. However, after a longer storing time, here the RBCs start to deform later (only deforming in regions where the cells' velocity is higher), only after the beginning of the contraction and for a shorter distance, and also recovering their original shape immediately after the end of the contraction, with no second deformation peak in the 400–600 μm interval, presenting a behavior similar to the one previously discussed for the RBC + Fe-MNPs samples after 1 h. Thus, after 72 h, all samples have a more similar behavior (when compared to the results after 1 h), indicating that the increase of the RBCs rigidity over time may have a higher influence in the DI results than the nanoparticles binding.

It is also important to notice that the previously presented curves represent randomly selected individual RBCs. For a global analysis of the results, Table 1 and Table 2 present the mean and standard deviation data ($n = 10$) of the maximum deformability and velocity in the microchannel, respectively, for all the samples. Statistical analysis was performed using GraphPad Prism 9.00 (Graph-Pad Software, Inc.). One-way ANOVA was used to assess the statistical significance of each sample, where all samples at 1 h storing time were compared against the healthy RBC sample at 1 h, and all samples at 72 h storing time were compared against the same sample at 1 h storing time. Statistical significance was recognized for $p \leq 0.05$.

The mean data shows the same tendency as the individual RBCs presented in Figs. 5 and 6 plots. RBCs with magnetic Fe-MNPs have lower deformability ($\leq$0.8) than the healthy and non-magnetic Ce-NPs RBCs (average $\geq$ 0.8). Also, as expected, the maximum deformation reached by the RBCs is always higher 1 h than 72 h after sample preparation. Thus, the lowest average DI (0.72) was obtained for the RBCs from the 72-hour old sample with 0.1 % Fe-MNPs. Furthermore, the DI standard deviation is low in all cases, but slightly higher in the magnetic Fe-MNPs (up to $\pm$ 0.04). Regarding the velocities, the average maximum velocity reached by the RBCs at the end of the contraction stands between 60 and 75 cm/s. In theory, the velocity should be similar for all samples and storing times. However, some variations were observed, since, when evaluating individual RBCs, the DI and velocity values are obtained through a laborious and manual work of individual cells' selection, tracking and analysis. Thus, when performing RBCs evaluation, there is the possibility of human error, namely when assuring that all the selected cells from all samples are in the same height plan in the microchannel, exactly at the same distance from the microchannel walls. If RBCs from a different plan are selected, since they may be positioned at different distances from the substrate or the top of the microchannel, small variations in the measured cell velocity are expected.

3.2. Deformation index vs velocity

After evaluating the DI and velocity for all the samples, the DI was also considered as a function of velocity. This allows to assess the effect of the extensional flow in the deformation of the cells, i.e., although the flow rate is constant from the syringe pump, when the RBCs flow through the hyperbolic contraction, the velocities are not constant but rather increase linearly which promotes a constant strain rate. For that

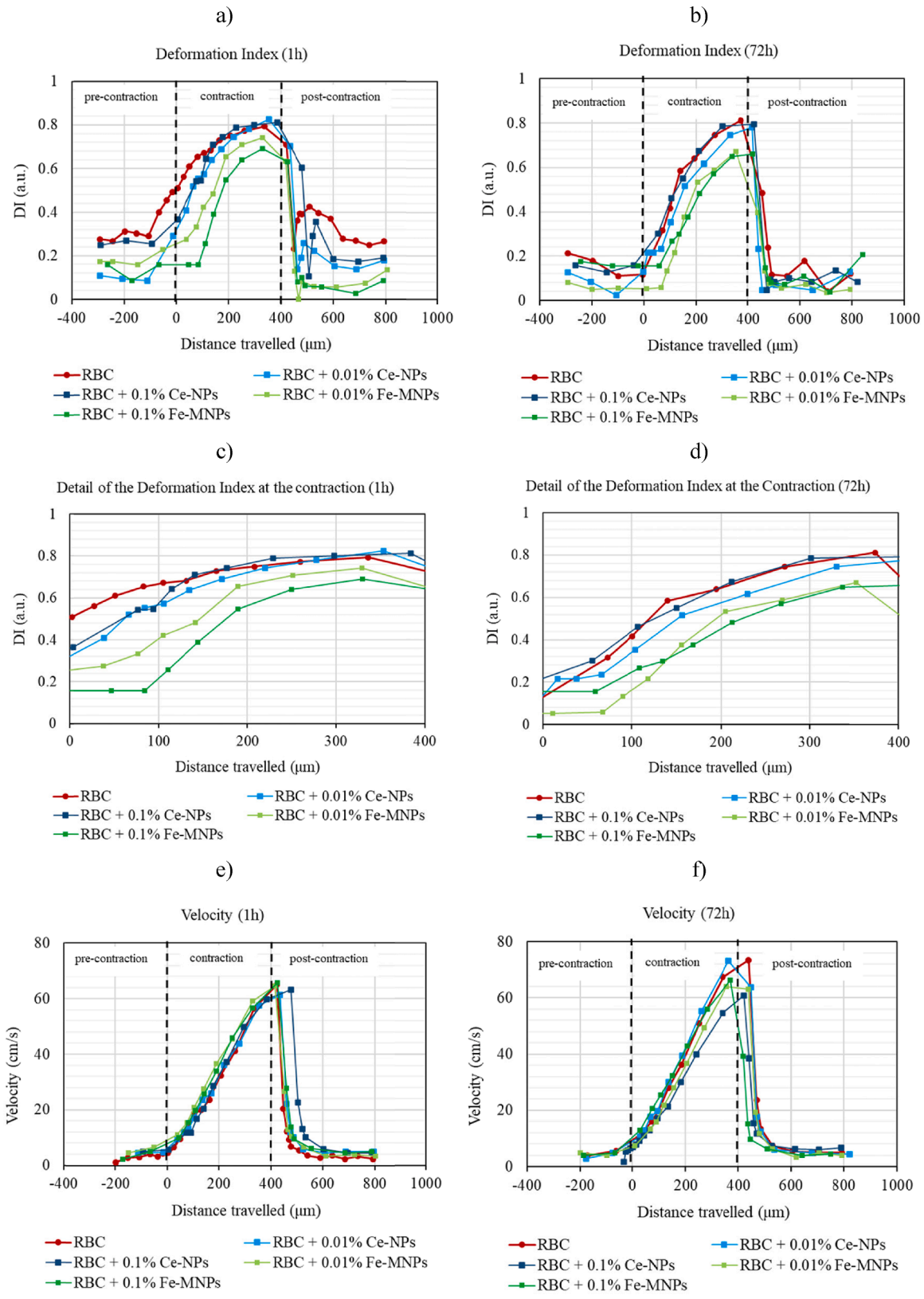

Fig. 5. Example of the Deformation Index (a.u.) and particle velocity (cm/s) of a randomly selected RBC as a function of the distance travelled through the hyperbolic contraction (μm) for the healthy RBCs (red series), RBC + 0.01 % Ce-NPs (light blue), RBC + 0.1 % Ce-NPs (dark blue), RBC + 0.01 % Fe-MNPs (light green) and RBC + 0.1 % Fe-MNPs (dark green) samples: **a)** DI 1 h after sample preparation; **b)** DI 72 h after sample preparation; **c)** Detail of the DI in the contraction region, 1 h after sample preparation; **d)** Detail of the DI in the contraction region, 72 h after sample preparation; **e)** velocity 1 h after sample preparation; **f)** velocity 72 h after sample preparation. For a better analysis of the results, the vertical dashed lines represent the start and end positions of the geometric contraction.

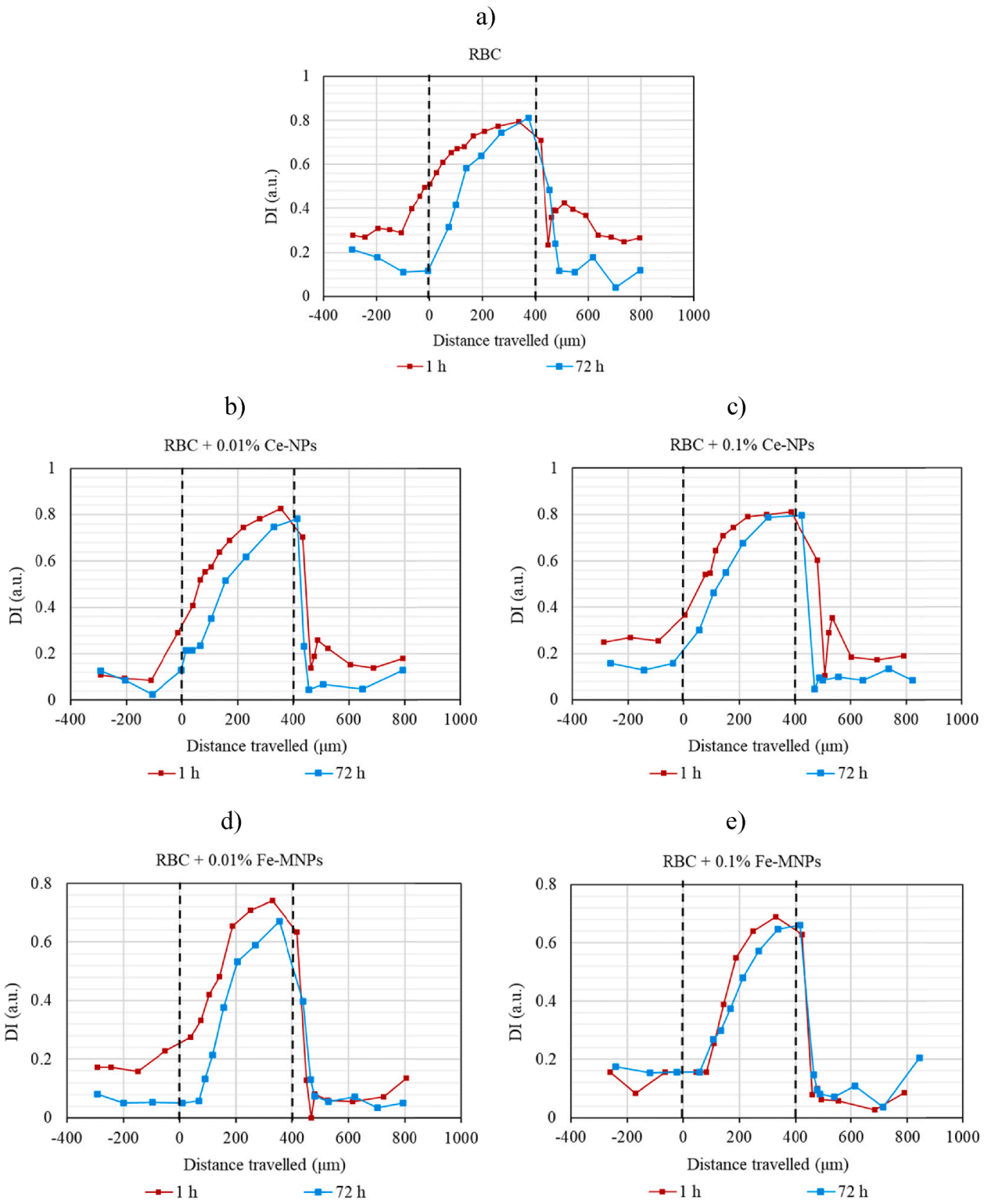

Fig. 6. Comparison between the Deformation Index (a.u.) of randomly selected RBCs, as a function of the distance travelled through the hyperbolic contraction (μm), at 1 h and 72 h after samples preparation: **a)** RBC; **b)** RBC + 0.01 % Ce-NPs; **c)** RBC + 0.1 % Ce-NPs; **d)** RBC + 0.01 % Fe-MNPs; **e)** RBC + 0.1 % Fe-MNPs. For a better analysis of the results, the vertical dashed lines represent the start and end positions of the geometric contraction.

purpose, Fig. 7 presents diagrams compiling all data of RBCs velocity and the respective DI at the same positions in the channel (sample size n = 10 RBCs), 1 h (Fig. 7a)) and 72 h (Fig. 7b)) after sample preparation, as well as the evaluation of the maximum DI and velocity of each of the analyzed RBCs (Fig. 7c)). It is relevant to note that only measurements up to the end of the contraction were considered, so no points in the recovery area were taken into account. In Supporting Information, they are available the individual RBCs plots for each sample, both at 1 h and 72 h, showing that the DI vs velocity trend remains the same among the RBCs from the same type of sample.

Even though the maximum DI reached at the end is around 0.8 for almost all samples (as previously observed in Table 1), it is noticeable

Table 1
Mean and standard deviation values of the maximum Deformation Index (a.u.) in the microchannel, calculated from 10 samples ($n = 10$), measured 1 h and 72 h after sample preparation. Statistical significance (*) was recognized for $p \leq 0.05$.

Maximum DI in the channel (a.u.) ($n = 10$)						
Samples	**1 h**			**72 h**		
	Mean	**Standard deviation**	**p-value**	**Mean**	**Standard deviation**	**p-value**
RBC	0.82	± 0.02	–	0.8	± 0.02	0.2875
RBC + 0.01 % Ce-NPs	0.82	± 0.02	0.8176	0.8	± 0.03	0.3273
RBC + 0.1 % Ce-NPs	0.83	± 0.02	0.5294	0.82	± 0.02	0.7347
RBC + 0.01 % Fe-MNPs	0.78	± 0.04	0.0746	0.76	± 0.04	0.9188
RBC + 0.1 % Fe-MNPs	0.8	± 0.03	0.8563	0.71	± 0.04	0.0002*

Table 2
Mean and standard deviation values of the maximum velocity in the microchannel (cm/s), calculated from 10 samples ($n = 10$), measured 1 h and 72 h after sample preparation. Statistical significance (*) was recognized for $p \leq 0.05$.

Maximum velocity in the channel (cm/s) ($n = 10$)						
Samples	**1 h**			**72 h**		
	Mean	**Standard deviation**	**p-value**	**Mean**	**Standard deviation**	**p-value**
RBC	60.13	± 6.94	–	74.33	± 7.76	0.0053*
RBC + 0.01 % Ce-NPs	62.39	± 4.89	0.9342	74.76	± 3.47	0.0006*
RBC + 0.1 % Ce-NPs	68.07	± 1.96	0.0086*	70.22	± 4.30	0.5882
RBC + 0.01 % Fe-MNPs	66.81	± 7.12	0.0844	69.22	± 6.02	0.9666
RBC + 0.1 % Fe-MNPs	68.02	± 5.26	0.1747	62.93	± 3.38	0.1409

that, after 1 h, the RBCs samples assume much higher DIs in the initial range of velocities than after 72 h. Additionally, after 1 h (Fig. 7a)), it is observed a progression from healthy RBCs (red series) to non-magnetic Ce-NPs (blue series) and magnetic Fe-MNPs (green series), which is in agreement with all the previous results and shows the biggest difficulty of the RBCs + Fe-MNPs to deform (due to the higher amount of binding of these NPs in the RBCs). We can also observe that, after 72 h, the behavior is much similar between all samples.

Once again, the differences between Fig. 7a) and b) show that the time spent after the sample preparation affects the deformability of the RBCs. Healthy RBCs samples are the ones with the highest difference over time. As the RBCs become less deformable over time, they need higher velocities to achieve similar deformation values. Fig. 8 details, for each sample, the DI vs velocity relation and trendlines for 1 h and 72 h after sample preparation ($n = 10$), and the results are in agreement with the previously discussed. Overall, after 1 h, for all samples, the DI increases logarithmically with the increase of velocity. However, after 72 h, the DI modifies its trend. In particular, for the RBCs + 0.1 % Fe-MNPs sample, the DI vs velocity relation loses the logarithmic trend, approaching a polynomial curve.

Since data evaluation and manual image analysis are very time-consuming, only 10 RBCs were tracked per sample, which is, indeed, a small amount, when compared to the total amount of RBCs flowing in the microchannels. However, based on the presented results, where each series is based on the tracking of 10 different RBCs ($n = 10$), we observe that the 10 randomly selected RBCs seem enough to represent the deformation behavior of the cells in the microdevice, as they all show a similar trend in Fig. 8 (in each sample, the RBCs data superimposes on the same curve). Another reason is a relatively small standard deviation of maximum DI and velocity, as seen in Tables 1 and 2. Thus, although the results previously presented in Figs. 5 and 6 represent the tracking of individual RBCs, the mechanical behavior of the cells is similar to their mean behavior.

4. Conclusions

Microfluidic devices with geometric contractions have the potential to create extensional flows, able to characterize the impact of several diseases, such as malaria or diabetes, by assessing the DI variation of the individual RBCs [4,45,53]. In addition, as shown in this work, these devices have the ability to evaluate the effects of different nanocarriers when interacting with blood cells [23].

This work reported the deformation behavior of healthy RBCs with and without two different kinds of nanocarriers: magnetic Fe-MNPs and non-magnetic Ce-NPs having a diameter of about 20 nm. The results showed that, in the hyperbolic contraction used in the flow experiments, and under a controlled extensional flow, the RBCs DI is strongly dependent on the cells' velocity at the microchannel contraction. Additionally, the average maximum DI achieved by healthy RBCs in contact with Fe-MNPs was lower than in contact with Ce-NPs, confirming the lower deformation capacity of RBCs in contact with the magnetic NPs. One hypothesis for this difference relies on the strongest electrostatic interactions between the positively charged Fe-MNPs and the negatively charged RBCs' membranes, when compared to the negatively charged Ce-NPs. On a minor contribution, it is also possible that some differences may occur due to the presence of a magnetic interaction of the MNPs with the high iron content in the RBCs (due to the presence of hemoglobin). However, further studies need to be conducted to fully understand this phenomenon and to validate this hypothesis. Additionally, plotting the DI as a function of the velocity seems to be a promising method to compare the deformation behavior of RBCs under different conditions. The results also showed that, regarding the deformability of the cells, storing RBCs outside plasma (even keeping them in D×40) leads, over time, to a significant loss of the cells' natural properties. Consequently, these types of experimental analysis should always be performed as soon as possible, with fresher RBCs samples and shorter storing times.

Regarding the impact of this work, NPs have demonstrated, in the last years, enormous potential as effective drug delivery vehicles [16,54–57]. However, several challenges still need to be addressed. On one hand, nanocarriers must assure that drug doses are administered locally and in quantities sufficient to eliminate the pathogens quickly, and on the other hand, the total doses must be sufficiently low to have no side effects on the human host. Both goals can be achieved simultaneously through targeted drug delivery strategies using nanocarriers [56–60], carrying binding molecules for specific receptors or benefiting from properties of the cells (as their paramagnetic properties). However, both the NPs concentration and the contact time had a significant effect on the RBCs deformability. Rigid RBCs can cause coagulation phenomena in the microcirculation vessels (i.e. capillaries, arterioles and venules) leading to blockage of normal blood flow in microcirculation [61], which, in the worst case, can result in ischemia in the tissues and/or cerebrovascular accidents [47]. Thus, this risk needs to be studied. Nevertheless, in this work, the working fluid contained 0.01 % and 0.1 % NPs in 0.1 % hematocrit, which is an extremely high NPs/RBCs ratio, a ratio unlikely to be used in *in vitro* drug assays. Although it is expected

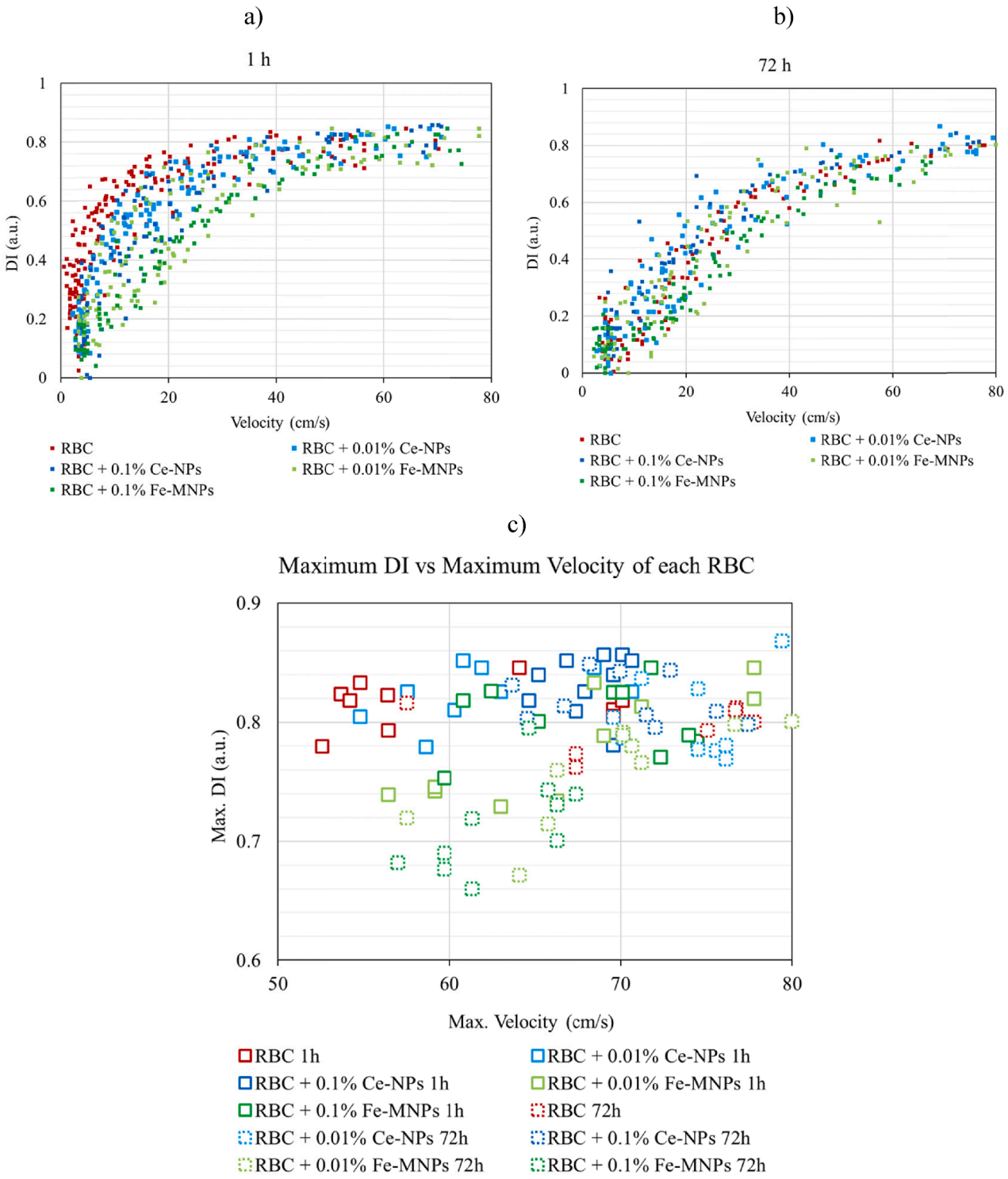

Fig. 7. Deformation Index (a.u.) as a function of cell velocity (cm/s) for 10 randomly selected RBCs, for the healthy RBCs (red series), RBC + 0.01 % Ce-NPs (light blue), RBC + 0.1 % Ce-NPs (dark blue), RBC + 0.01 % Fe-MNPs (light green) and RBC + 0.1 % Fe-MNPs (dark green) samples: **a)** 1 h after sample preparation; **b)** 72 h after sample preparation; **c)** Maximum Deformation Index and the correspondent maximum velocity for each individual RBC under analysis. Each datapoint represents the DI that one specific RBC had at the corresponding velocity.

that the NPs concentration in vitro will potentially be much lower, leading to a less pronounced effect on the RBCs DI, studying these high concentrations of NPs allows us to understand how the cells behave in such extreme conditions, still being able to deform (DI > 0.7 in all experiments, even after 72 h). So, these results open new research possibilities, regarding the study of magnetic NPs in diagnosis and therapeutics, as well as the integration of such nano systems in microfluidic, lab-on-a-chip and organ-on-a-chip devices [62,63].

Declaration of Competing Interest

The authors declare that they have no known competing financial interests or personal relationships that could have appeared to influence the work reported in this paper.

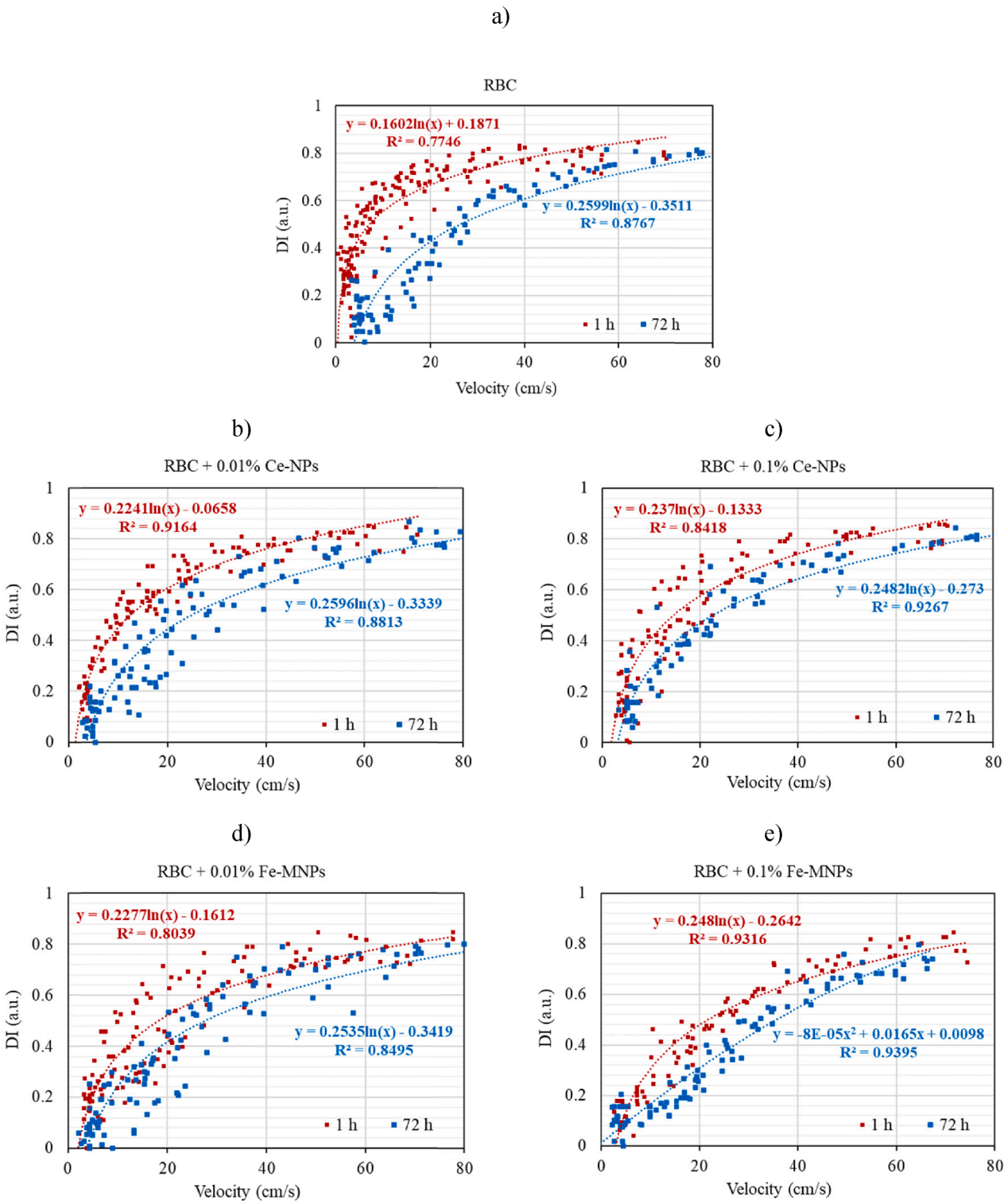

Fig. 8. Deformation Index (a.u.) as a function of cell velocity (cm/s) for 10 randomly selected RBCs, 1 h (red series) and 72 h (blue series) after sample preparation, for: **a)** healthy RBCs; **b)** RBC + 0.01 % Ce-NPs; **c)** RBC + 0.1 % Ce-NPs; **d)** RBC + 0.01 % Fe-MNPs; **e)** RBC + 0.1 % Fe-MNPs. Each datapoint represents the DI that one specific RBC had at the corresponding velocity.

Data availability

Data will be made available on request.

Acknowledgement

This work has been supported by the project PTDC/EEI-EEE/2846/2021, funded by national funds (OE), within the scope of the Scientific Research and Technological Development Projects (IC&DT) program in all scientific domains (PTDC), through the Fundação para a Ciência e Tecnologia (FCT, I.P). The authors also acknowledge the partial financial support within the R&D Units Projects Scope: UIDB/04436/2020, UIDP/04436/2020, UIDB/04077/2020, UIDB/00532/2020 and LA/P/0045/2020 (ALiCE) supported by FCT. Inês M. Gonçalves and Vitória

Baptista acknowledge the PhD scholarships BD/08646/2020 and SFRH/BD/145427/2019, respectively, attributed by FCT. Maria Isabel Veiga and Susana O. Catarino thank FCT for their contracts funding provided through 2020.03113.CEECIND and 2020.00215.CEECIND, respectively. The authors acknowledge Professor Dr Ana Paula Ribeiro (Instituto Superior Técnico) for providing the non-magnetic nanoparticles for the experimental assays; Dr Paulo Sousa for the O2 plasma bonding; and Professor Dr Filipe Vaz (Centro de Física - CFUM) for the O2 plasma bonding equipment availability.

Appendix A. Supplementary material

Supplementary data to this article can be found online at https://doi.org/10.1016/j.expthermflusci.2023.110931.

References

[1] K. Tsuda, Red blood cell abnormalities and hypertension, Hypertens. Res. 43 (2020) 72–73, https://doi.org/10.1038/s41440-019-0353-0.
[2] G. Mchedlishvili, N. Maeda, Blood flow structure related to red cell flow: Determinant of blood fluidity in narrow microvessels, Jpn. J. Physiol. 51 (2001) 19–30, https://doi.org/10.2170/jjphysiol.51.19.
[3] A.M. Dondorp, P.A. Kager, J. Vreeken, N.J. White, Abnormal blood flow and red blood cell deformability in severe malaria, Parasitol. Today 16 (2000) 228–232, https://doi.org/10.1016/S0169-4758(00)01666-5.
[4] D. Pinho, V. Faustino, S.O. Catarino, A.I. Pereira, G. Minas, F.T. Pinho, R. Lima, Label-free multi-step microfluidic device for mechanical characterization of blood cells: Diabetes type II, Micro Nano Eng. 16 (2022), 100149, https://doi.org/10.1016/j.mne.2022.100149.
[5] A. Vayá, L. Rivera, R. de la Espriella, F. Sanchez, M. Suescun, J.L. Hernandez, L. Fácila, Red blood cell distribution width and erythrocyte deformability in patients with acute myocardial infarction, Clin. Hemorheol. Microcirc. 59 (2015) 107–114, https://doi.org/10.3233/CH-131751.
[6] E. Nader, M. Romana, P. Connes, The red blood cell—inflammation vicious circle in sickle cell disease, Front. Immunol. 11 (2020), https://doi.org/10.3389/fimmu.2020.00454.
[7] R. Lima, T. Ishikawa, Y. Imai, T. Yamaguchi, in: Blood flow behavior in microchannels: Past, current and future trends, Bentham science, 2012, pp. 513–547. ISBN 978-1-60805-295-0.
[8] A.C. Burton, On the physical equilibrium of small blood vessels, Am. J. Physiol. Content 164 (1951) 319–329, https://doi.org/10.1152/ajplegacy.1951.164.2.319.
[9] S.E. Francis, D.J. Sullivan, D.E. Goldberg, Hemoglobin metabolism in the malaria parasite plasmodium falciparium, Annu. Rev. Microbiol. 51 (1997) 97–123, https://doi.org/10.1146/annurev.micro.51.1.97.
[10] D. Zhang, D. Fan, Multidrug resistance in gastric cancer: Recent research advances and ongoing therapeutic challenges, Expert Rev. Anticancer Ther. 7 (2007) 1369–1378, https://doi.org/10.1586/14737140.7.10.1369.
[11] C. Lee, Therapeutic challenges in the era of antibiotic resistance, Int. J. Antimicrob. Agents 32 (2008) S197–S199, https://doi.org/10.1016/S0924-8579(09)70002-0.
[12] C.V. Plowe, Malaria chemoprevention and drug resistance: A review of the literature and policy implications, Malar. J. 21 (2022) 104, https://doi.org/10.1186/s12936-022-04115-8.
[13] W. Gao, J.M. Chan, O.C. Farokhzad, PH-responsive nanoparticles for drug delivery, Mol. Pharm. 7 (2010) 1913–1920, https://doi.org/10.1021/mp100253e.
[14] S. Morarasu, B.C. Morarasu, R. Ghiarasim, A. Coroaba, C. Tiron, R. Iliescu, G.-M. Dimofte, Targeted cancer therapy via PH-functionalized nanoparticles: A scoping review of methods and outcomes, Gels 8 (2022) 232, https://doi.org/10.3390/gels8040232.
[15] T.S. Anirudhan, A.S. Nair, Temperature and ultrasound sensitive gatekeepers for the controlled release of chemotherapeutic drugs from mesoporous silica nanoparticles, J. Mater. Chem. B 6 (2018) 428–439, https://doi.org/10.1039/C7TB02292A.
[16] L. Neves Borgheti-Cardoso, M. San Anselmo, E. Lantero, A. Lancelot, J.L. Serrano, S. Hernández-Ainsa, X. Fernàndez-Busquets, T. Sierra, Promising nanomaterials in the fight against malaria, J. Mater. Chem. B 8 (2020) 9428–9448, https://doi.org/10.1039/D0TB01398F.
[17] F. Sharifianjazi, M. Irani, A. Esmaeilkhanian, L. Bazli, M.S. Asl, H.W. Jang, S. Y. Kim, S. Ramakrishna, M. Shokouhimehr, R.S. Varma, Polymer incorporated magnetic nanoparticles: Applications for magnetoresponsive targeted drug delivery, Mater. Sci. Eng. B 272 (2021), 115358, https://doi.org/10.1016/j.mseb.2021.115358.
[18] L. Maldonado-Camargo, M. Unni, C. Rinaldi, Magnetic characterization of iron oxide nanoparticles for biomedical applications, Biomed. Nanotechnol. Method Protocol. (2017) 47–71, https://doi.org/10.1007/978-1-4939-6840-4_4.
[19] Y. Qiao, J. Wan, L. Zhou, W. Ma, Y. Yang, W. Luo, Z. Yu, H. Wang, Stimuli-responsive nanotherapeutics for precision drug delivery and cancer therapy, WIREs Nanomed. Nanobiotechnol. 11 (2019), https://doi.org/10.1002/wnan.1527.
[20] V. Baptista, M.S. Costa, C. Calçada, M. Silva, J.P. Gil, M.I. Veiga, S.O. Catarino, The future in sensing technologies for malaria surveillance: A review of hemozoin-based diagnosis, ACS Sens. 6 (2021) 3898–3911, https://doi.org/10.1021/acssensors.1c01750.
[21] B. Hawkett, B. Pham, N. Jain, P. Kuchel, B. Chapman, S. Bickley, S. Jones, The interaction of sterically stabilized magnetic nanoparticles with fresh human red blood cells, Int. J. Nanomed. 6645 (2015), https://doi.org/10.2147/IJN.S93225.
[22] D.E. Creangă, M. Culea, C. Nădejde, S. Oancea, L. Curecheriu, M. Racuciu, Magnetic nanoparticle effects on the red blood cells, J. Phys. Conf. Ser. 170 (2009), 012019, https://doi.org/10.1088/1742-6596/170/1/012019.
[23] R.O. Rodrigues, M. Bañobre-López, J. Gallo, P.B. Tavares, A.M.T. Silva, R. Lima, H. T. Gomes, Haemocompatibility of iron oxide nanoparticles synthesized for theranostic applications: A high-sensitivity microfluidic tool, J. Nanoparticle Res. 18 (2016) 194, https://doi.org/10.1007/s11051-016-3498-7.
[24] T. Lage, V. Faustino, R.O. Rodrigues, R.A. Lima, G. Minas, Haemocompatibility test of simple magnetic nanoparticles using the distribution of deformed RBCs, in: Proceedings of the 2019 IEEE 6th Portuguese meeting on bioengineering (ENBENG), IEEE, 2019, pp. 1–4, https://doi.org/10.1109/ENBENG.2019.8692543.
[25] K. Müller, D.A. Fedosov, G. Gompper, Margination of micro- and nano-particles in blood flow and its effect on drug delivery, Sci. Rep. 4 (2015) 4871, https://doi.org/10.1038/srep04871.
[26] A. Mayer, M. Vadon, B. Rinner, A. Novak, R. Wintersteiger, E. Fröhlich, The role of nanoparticle size in hemocompatibility, Toxicology 258 (2009) 139–147, https://doi.org/10.1016/j.tox.2009.01.015.
[27] A. Hervault, N.T.K. Thanh, Magnetic nanoparticle-based therapeutic agents for thermo-chemotherapy treatment of cancer, Nanoscale 6 (2014) 11553–11573, https://doi.org/10.1039/C4NR03482A.
[28] J. Rivas, M. Bañobre-López, Y. Piñeiro-Redondo, B. Rivas, M.A. López-Quintela, Magnetic nanoparticles for application in cancer therapy, J. Magn. Magn. Mater. 324 (2012) 3499–3502, https://doi.org/10.1016/j.jmmm.2012.02.075.
[29] T.D. Mai, F. D'Orlyé, C. Ménager, A. Varenne, J.-M. Siaugue, Red blood cells decorated with functionalized core-shell magnetic nanoparticles: Elucidation of the adsorption mechanism, Chem. Commun. 49 (2013) 5393, https://doi.org/10.1039/c3cc41513a.
[30] J. Nowak-Jary, B. Machnicka, Pharmacokinetics of magnetic iron oxide nanoparticles for medical applications, J. Nanobiotechnol. 20 (2022) 305, https://doi.org/10.1186/s12951-022-01510-w.
[31] A. Dias, M. Werner, K.R. Ward, J.-B. Fleury, V.A. Baulin, High-throughput 3D visualization of nanoparticles attached to the surface of red blood cells, Nanoscale 11 (2019) 2282–2288, https://doi.org/10.1039/C8NR09960J.
[32] B.M. Rothen-Rutishauser, S. Schürch, B. Haenni, N. Kapp, P. Gehr, Interaction of fine particles and nanoparticles with red blood cells visualized with advanced microscopic techniques, Environ. Sci. Technol. 40 (2006) 4353–4359, https://doi.org/10.1021/es0522635.
[33] Y. Ikeda, H. Nakamura, S. Ohsaki, S. Watano, Direct translocation of a negatively charged nanoparticle across a negatively charged model cell membrane, Phys. Chem. Chem. Phys. 23 (2021) 10591–10599, https://doi.org/10.1039/D0CP06278B.
[34] K.L. Bren, R. Eisenberg, H.B. Gray, Discovery of the magnetic behavior of hemoglobin: A beginning of bioinorganic chemistry, Proc. Natl. Acad. Sci. 112 (2015) 13123–13127, https://doi.org/10.1073/pnas.1515704112.
[35] L. Pauling, C.D. Coryell, The magnetic properties and structure of hemoglobin, oxyhemoglobin and carbonmonoxyhemoglobin, Proc. Natl. Acad. Sci. 22 (1936) 210–216, https://doi.org/10.1073/pnas.22.4.210.
[36] Z. Mhlwatika, B. Aderibigbe, Polymeric nanocarriers for the delivery of antimalarials, Molecules 23 (2018) 2527, https://doi.org/10.3390/molecules23102527.
[37] C. Fan, J. Joshi, F. Li, B. Xu, M. Khan, J. Yang, W. Zhu, Nanoparticle-mediated drug delivery for treatment of ischemic heart disease, Front. Bioeng. Biotechnol. 8 (2020), https://doi.org/10.3389/fbioe.2020.00687.
[38] F. Yang, J. Xue, G. Wang, Q. Diao, Nanoparticle-based drug delivery systems for the treatment of cardiovascular diseases, Front. Pharmacol. (2022,) 13, https://doi.org/10.3389/fphar.2022.999404.
[39] X. Yang, P. Ma, Q. Luo, J. Chen, Y. Gan, J. Du, S. Ding, Z. Xi, Intraperitoneal injection of magnetic fe3o4-nanoparticle induces hepatic and renal tissue injury via oxidative stress in mice, Int. J. Nanomedicine 4809 (2012), https://doi.org/10.2147/IJN.S34349.
[40] W.E. Mahmoud, A. Faidah, Microwave assisted hydrothermal synthesis of engineered cerium oxide nanopowders, J. Eur. Ceram. Soc. 32 (2012) 3537–3541, https://doi.org/10.1016/j.jeurceramsoc.2012.05.003.
[41] D. Parimi, V. Sundararajan, O. Sadak, S. Gunasekaran, S.S. Mohideen, A. Sundaramurthy, Synthesis of positively and negatively charged CeO 2 nanoparticles: Investigation of the role of surface charge on growth and development of drosophila melanogaster, ACS Omega 4 (2019) 104–113, https://doi.org/10.1021/acsomega.8b02747.
[42] T.Z. Mehrizi, Hemocompatibility and hemolytic effects of functionalized nanoparticles on red blood cells: A recent review study, Nano 16 (2021) 2130007, https://doi.org/10.1142/S1793292021300073.
[43] V. Agarwal, V. Gupta, V.K. Bhardwaj, K. Singh, P. Khullar, M.S. Bakshi, Hemolytic response of iron oxide magnetic nanoparticles at the interface and in bulk: Extraction of blood cells by magnetic nanoparticles, ACS Appl. Mater. Interfaces 14 (2022) 6428–6441, https://doi.org/10.1021/acsami.1c23496.
[44] V. Pinto, P. Sousa, V. Cardoso, G. Minas, Optimized SU-8 processing for low-cost microstructures fabrication without cleanroom facilities, Micromachines 5 (2014) 738–755, https://doi.org/10.3390/mi5030738.
[45] V. Faustino, D. Pinho, S.O. Catarino, G. Minas, R.A. Lima, Geometry effect in multi-step crossflow microfluidic devices for red blood cells separation and deformability assessment, Biomed. Microdev. 24 (2022) 20, https://doi.org/10.1007/s10544-022-00616-0.

[46] D. Bento, R. Rodrigues, V. Faustino, D. Pinho, C. Fernandes, A. Pereira, V. Garcia, J. Miranda, R. Lima, Deformation of red blood cells, air bubbles, and droplets in microfluidic devices: Flow visualizations and measurements, Micromachines 9 (2018) 151, https://doi.org/10.3390/mi9040151.
[47] T. Yaginuma, M.S.N. Oliveira, R. Lima, T. Ishikawa, T. Yamaguchi, Human Red Blood Cell Behavior under Homogeneous Extensional Flow in a Hyperbolic-Shaped Microchannel, Biomicrofluidics 7 (2013), https://doi.org/10.1063/1.4820414.
[48] R. Reale, A.De. Ninno, T. Nepi, P. Bisegna, F. Caselli, Extensional-flow impedance cytometer for contactless and optics-free erythrocyte deformability analysis, IEEE Trans. Biomed. Eng. (2022) 1–9, https://doi.org/10.1109/TBME.2022.3197214.
[49] S.S. Lee, Y. Yim, K.H. Ahn, S.J. Lee, Extensional flow-based assessment of red blood cell deformability using hyperbolic converging microchannel, Biomed. Microdevices 11 (2009) 1021–1027, https://doi.org/10.1007/s10544-009-9319-3.
[50] M.S.N. Oliveira, M.A. Alves, F.T. Pinho, G.H. McKinley, Viscous flow through microfabricated hyperbolic contractions, Exp. Fluids 43 (2007) 437–451, https://doi.org/10.1007/s00348-007-0306-2.
[51] V. Faustino, R.O. Rodrigues, D. Pinho, E. Costa, A. Santos-Silva, V. Miranda, J. S. Amaral, R. Lima, A microfluidic deformability assessment of pathological red blood cells flowing in a hyperbolic converging microchannel, Micromachines 10 (2019) 645, https://doi.org/10.3390/mi10100645.
[52] L. Boas, V. Faustino, R. Lima, J. Miranda, G. Minas, C. Fernandes, S. Catarino, Assessment of the deformability and velocity of healthy and artificially impaired red blood cells in narrow polydimethylsiloxane (PDMS) microchannels, Micromachines 9 (2018) 384, https://doi.org/10.3390/mi9080384.
[53] V. Faustino, S. Catarino, D. Pinho, R. Lima, G. Minas, A passive microfluidic device based on crossflow filtration for cell separation measurements: A spectrophotometric characterization, Biosensors 8 (2018) 125, https://doi.org/10.3390/bios8040125.
[54] M.J. Mitchell, M.M. Billingsley, R.M. Haley, M.E. Wechsler, N.A. Peppas, R. Langer, Engineering precision nanoparticles for drug delivery, Nat. Rev. Drug Discov. 20 (2021) 101–124, https://doi.org/10.1038/s41573-020-0090-8.
[55] B. Begines, T. Ortiz, M. Pérez-Aranda, G. Martínez, M. Merinero, F. Argüelles-Arias, A. Alcudia, Polymeric nanoparticles for drug delivery: Recent developments and future prospects, Nanomaterials 10 (2020) 1403, https://doi.org/10.3390/nano10071403.
[56] T. Zou, W. Lu, Y. Mezhuev, M. Lan, L. Li, F. Liu, T. Cai, X. Wu, Y. Cai, A Review of nanoparticle drug delivery systems responsive to endogenous breast cancer microenvironment, Eur. J. Pharm. Biopharm. 166 (2021) 30–43, https://doi.org/10.1016/j.ejpb.2021.05.029.
[57] A. Dadwal, A. Baldi, R. Kumar Narang, Nanoparticles as carriers for drug delivery in cancer, Artif. Cell. Nanomed. Biotechnol. 46 (2018) 295–305, https://doi.org/10.1080/21691401.2018.1457039.
[58] J. Pelt, S. Busatto, M. Ferrari, E.A. Thompson, K. Mody, J. Wolfram, Chloroquine and nanoparticle drug delivery: A promising combination, Pharmacol. Ther. 191 (2018) 43–49, https://doi.org/10.1016/j.pharmthera.2018.06.007.
[59] N. Puttappa, R.S. Kumar, G. Kuppusamy, A. Radhakrishnan, Nano-facilitated drug delivery strategies in the treatment of plasmodium infection, Acta Trop. 195 (2019) 103–114, https://doi.org/10.1016/j.actatropica.2019.04.020.
[60] S. Tripathy, S. Roy, a review of age-old antimalarial drug to combat malaria: Efficacy up-gradation by nanotechnology based drug delivery, Asian Pac. J. Trop. Med. 7 (2014) 673–679, https://doi.org/10.1016/S1995-7645(14)60115-2.
[61] Y.J. Kang, Y.-R. Ha, S.-J. Lee, Deformability measurement of red blood cells using a microfluidic channel array and an air cavity in a driving syringe with high throughput and precise detection of subpopulations, Analyst 141 (2016) 319–330, https://doi.org/10.1039/C5AN01988E.
[62] G.M.H. Minas, S.O. Catarino, in: Lab-on-a-chip devices for chemical analysis, Encyclopedia of microfluidics and nanofluidics, Springer, New York, New York, NY, 2015, pp. 1511–1531, https://doi.org/10.1007/978-1-4614-5491-5_774.
[63] S. Catarino, R. Lima, G. Minas, in: Smart devices, Bioinspired materials for medical applications, Elsevier, 2017, pp. 331–369, https://doi.org/10.1016/B978-0-08-100741-9.00012-7.